nature communications

Article | Article in Press

https://doi.org/10.1038/s41467-026-79291-1

Low-temperature operation of Ag–C based anodeless all-solid-state pouch cells

Received: 23 December 2025

Accepted: 14 October 2026

Published online: 18 November 2026

Check for updates

Hwiho Kim[1,6], Sebastian Kunze[1,2,6], Kyungho Yoon[3,6], Sooseong Hwang[1], Yujeong Hwang[1], Jiseok Kim[1], Dongil Kang[3], Ikcheon Na[1], Chih-Wen Pao[4], Wei-Hsiang Huang[4,5], Yong-Gun Lee[3], Jun Hwan Ku[3] ✉ & Jongwoo Lim[1] ✉

Anodeless all-solid-state batteries with Ag-C interlayers offer high energy density and long cycle life, yet their operation in cold environments remains limited by poorly understood failure mechanisms. Using operando X-ray absorption spectroscopy, cryogenic-cross-section electron microscopy, and X-ray diffraction, we discover that Li-Ag alloying dynamics are highly temperature-dependent: rapid at 45 °C but kinetically suppressed at 5 °C. At low temperatures, suppressed alloying leads to sluggish lithium transport, internal lithium extrusion, interlayer delamination, and rapid capacity decay. We demonstrate that a brief initial charge at 45 °C permanently activates the interlayer via Li-Ag alloy formation, enabling efficient Li transport even at 5 °C. Full pouch cells following this activation protocol retain 87% of their initial capacity after 250 completed cycles following one formation cycle at 5 °C, showing a threefold capacity improvement over fixed-temperature cycling. Such in situ electrochemical alloy activation offers a practical and scalable approach to extend anodeless all-solid-state battery performance to sub-ambient temperatures without material redesign.

Viable low-temperature operation of solid-state batteries with high energy density is an important scientific and practical challenge[1]. Anodeless all-solid-state batteries (AL-ASSBs) achieve high energy density by forming the lithium metal negative electrode in situ during charging, eliminating the need for pre-applied lithium metal foil[2]. However, without excess supply of lithium, their long-term performance can be compromised even by minute losses of Li inventory, therefore requiring reversible lithium plating and stripping. Achieving such high reversibility and coulombic efficiency is a grand challenge, as lithium metal readily reacts with the solid-state electrolyte (SSE) and plates inhomogeneously, which could be more severe during cold-weather operation[3].

Recently, it was discovered that introducing a functional Ag–C interlayer between the solid electrolyte and the negative electrode current collector enables extended cycle life of anodeless ASSBs. Such an interlayer comprises a carbon scaffold filled with dispersed Ag nanoparticles that undergo alloying with Li, mediating highly reversible and uniform Li deposition[4]. The microscale Ag–C interlayer is a mixed-ion-electron conductor (MIEC) that is stable against Li and the SSE, but also readily transports Li towards the current collector while spatially separating the resulting metallic Li deposits from the solid electrolyte, thus preventing the continuous formation of a solid-electrolyte interphase (SEI). Pouch cells employing this design have consequently demonstrated long cycle lives (>1000 cycles)[4].

However, the reported cycle life has been achieved exclusively at higher temperatures (T > 45 °C), where facile charge transfer, reduced nucleation potential and lower interfacial resistance promote uniform Li plating and stripping. Critically, the mechanistic role of the Ag–C

[1]Department of Chemistry, Seoul National University, 1 Gwanak-ro, Gwanak-gu, Seoul, Republic of Korea. [2]Research Institute for Basic Science, Seoul National University, 1 Gwanak-ro, Gwanak-gu, Seoul, Republic of Korea. [3]Samsung Advanced Institute of Technology (SAIT), Samsung Electronics Co., Ltd, Suwon, Korea. [4]National Synchrotron Radiation Research Center (NSRRC), Hsinchu, Taiwan. [5]Sustainable Electrochemical Energy Development (SEED) Center, National Taiwan University of Science and Technology, Taipei, Taiwan. [6]These authors contributed equally: Hwiho Kim, Sebastian Kunze, Kyungho Yoon. ✉e-mail: junhwan.ku@samsung.com; jwlim@snu.ac.kr

layer and how it enables reversible Li plating and stripping across wide climate conditions - particularly at sub-ambient temperatures where the kinetic advantages diminish - has not yet been elucidated, representing a key knowledge gap for real-world deployment[5].

The role of the Ag–C layer and how the lithium transport within the interlayer is modulated has been actively investigated in recent literature[6–13]. It has been discovered by in situ TEM studies that lithium transport through the carbon matrix is predominantly driven by Coble creep[14–16]. Additionally, facile Ag–Li alloying helps homogenize nucleation and transport of lithium[6,7,17,18]. The mechanism of Li plating underneath the carbon layer is proposed to proceed by a sequence of pore-filling of the Ag–C interlayer, followed by oversaturation of Li–Ag alloys and finally Li extrusion towards the current collector.

Because the interlayer assumes an active role in cell operation, these processes are very likely sensitive to the operating temperature of the cell, especially at industrially relevant moderate stack pressures and in larger cell formats such as pouch cells. The insights into the Ag–C dynamics so far have, however, been derived from half-cells and lab-scale cells, both of which deviate from real-world dynamics as well as application, with a lack of studies that investigate these dynamics in practical Ag–C-based full cells under demanding conditions such as in cold environments[5].

To clarify the mechanisms and behavior of Ag–C interlayers in anodeless full pouch cells under low temperatures, we resolved a longstanding experimental challenge in the operando analysis of ASSBs by maintaining stack pressure and temperature control while simultaneously providing X-ray access. Our platform ensured uniform pressure distribution with precise temperature control, enabling real-time observation of interlayer dynamics in pouch cells under practical operating conditions. We were thus able to perform complementary characterization methods, including operando quick-scanning extended X-ray absorption fine structure (QEXAFS), cryogenic cross-sectional polished scanning electron microscopy (CCP-SEM), and X-ray diffraction (XRD).

Our findings reveal that Li–Ag alloying in the Ag–C interlayer during first charge and lithium plating are both strongly temperature-dependent. Rapid alloy formation occurs at elevated temperatures (i.e., 45 °C), facilitating uniform lithium plating, while at low temperatures (i.e., 5 °C) alloying is suppressed, coinciding with structural degradation of the interlayer leading to severe capacity loss and cell failure. Notably, we further discovered that Li–Ag alloys, once formed, exhibit more facile Li transport through the Ag–C interlayer.

Based on the finding that the lithium transport properties of the Ag–C interlayer are intimately and permanently coupled to the formation conditions, we propose that an initial charge at 45 °C could activate the cells by promoting Li–Ag alloying (hereafter referred to as the 'alloy activation protocol') and condition them for subsequent low-temperature cycling. Even at 5 °C, such activated cells exhibited facile Li transport, favorable lithium deposition and preserved integrity of the interlayer, similar to cells cycled at high temperature. With this approach, we achieved 87% capacity retention after 250 completed cycles following one formation cycle in full pouch cells at 5 °C with an initial capacity of approximately 135 mAh/g compared to conventional

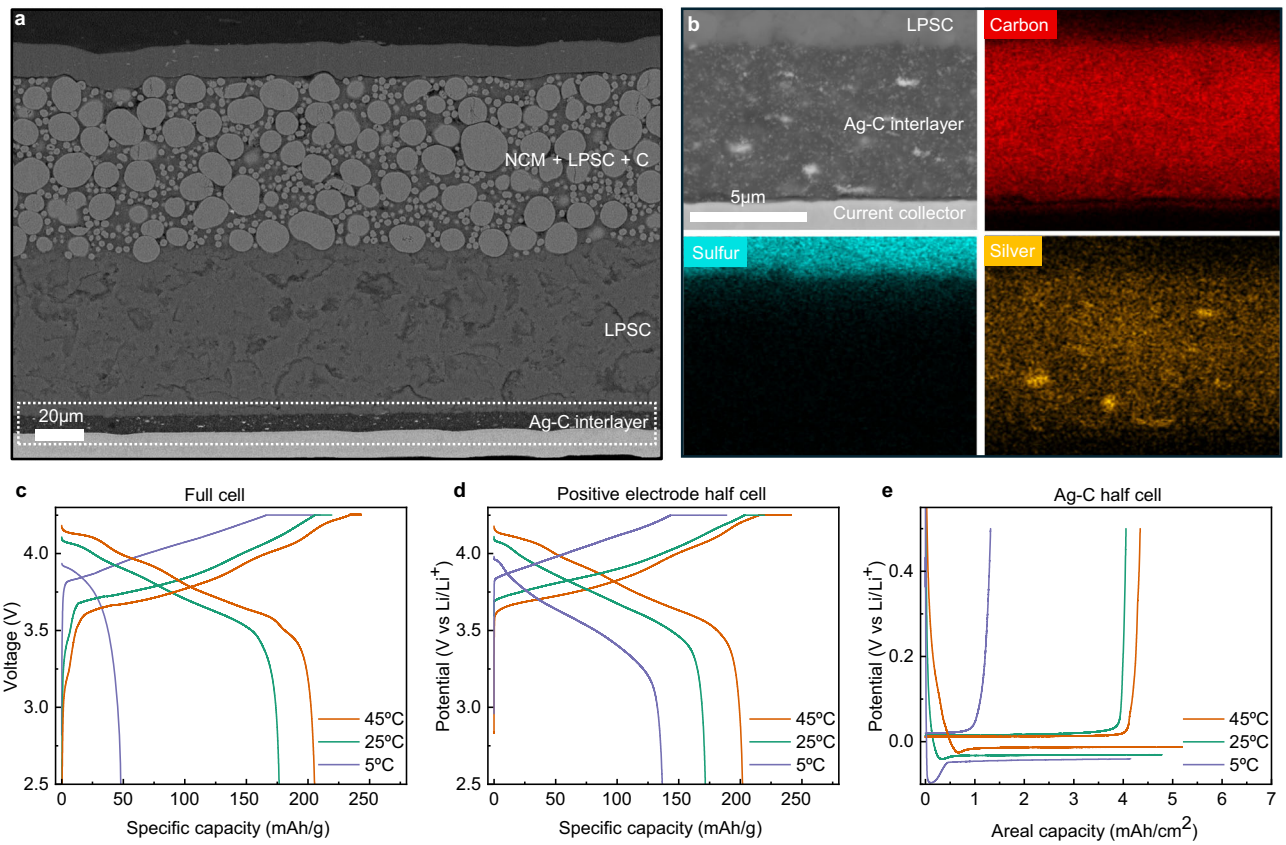


Fig. 1 | Full pouch cell configuration and voltage profiles of half and full cells. **a** CCP-SEM image of pristine anodeless pouch full cell. **b** Magnified Ag–C interlayer region and EDS maps, displaying spatial distributions of carbon, sulfur and silver. **c** The first-cycle voltage profile of pouch full cells at 45 °C, 25 °C, and 5 °C, respectively. **d** The first-cycle voltage profile of positive electrode half cells at 45 °C, 25 °C, and 5 °C, respectively. **e** The first-cycle voltage profile of negative electrode half cells at 45 °C, 25 °C, and 5 °C, respectively. All voltage profiles were recorded at a specific current of 40 mA/g, equivalent to a C-rate of 0.2 C (1 C corresponds to 4.2 mA/cm^2 or 200 mA/g) and stack pressures of 4 MPa. Charging steps (**c**) and **d** include a constant voltage step at 4.25 V until the current dropped to 20 mA/g. Abbreviations: Ag–C silver-carbon; CCP-SEM cryogenic cross-sectional polished scanning electron microscopy; EDS energy-dispersive X-ray spectroscopy; LPSC Li_6PS_5Cl solid electrolyte; NCM lithium nickel cobalt manganese oxide. In the EDS maps, carbon, sulfur, and silver are shown in red, cyan, and yellow, respectively.

https://doi.org/10.1038/s41467-026-79291-1

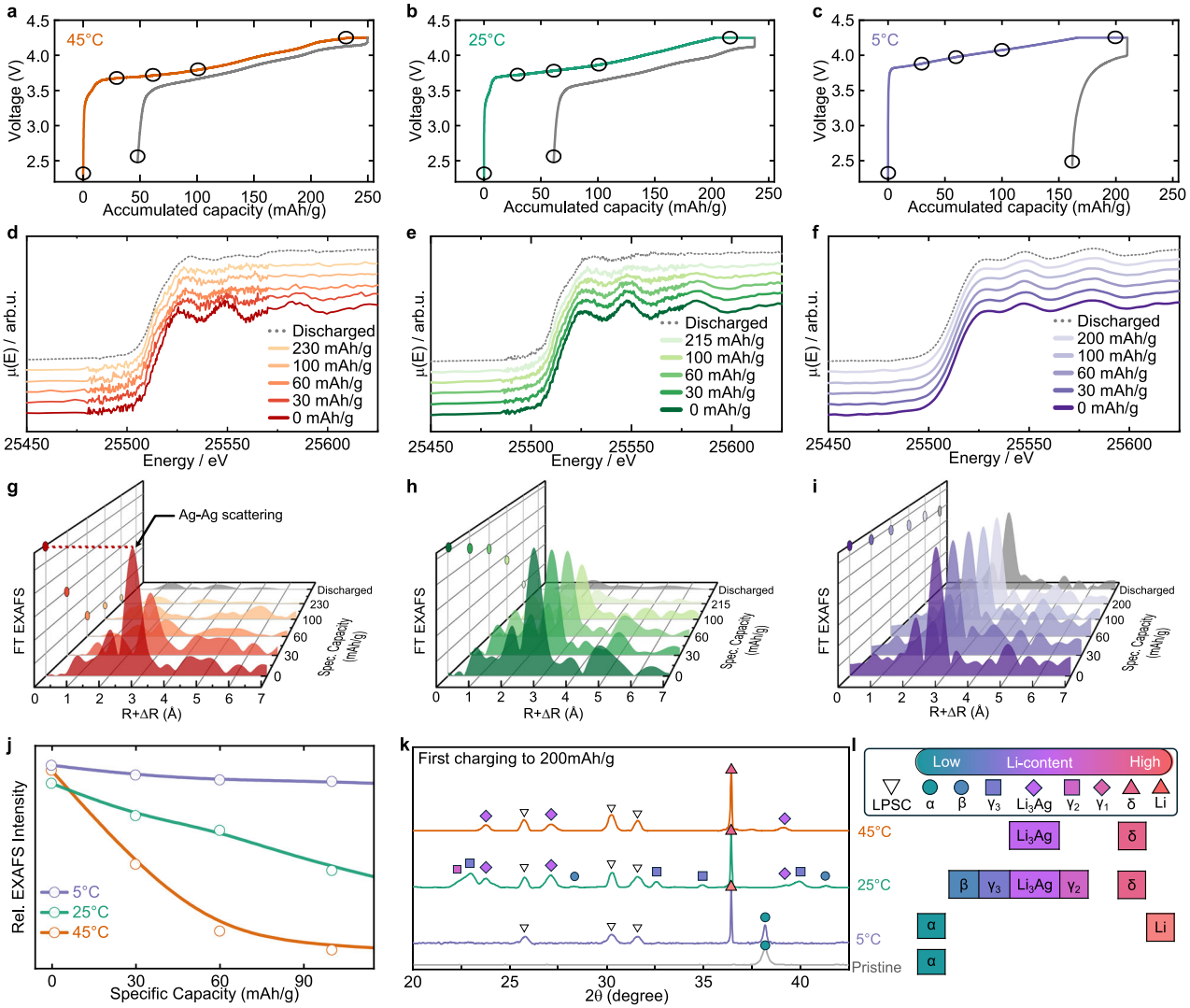


Fig. 2 | Operando QEXAFS and XRD investigation of AL-ASSB pouch cells at different temperatures. a–c First charge and discharge voltage profiles of pouch full cells during QEXAFS measurements. Circles mark the capacities of the corresponding EXAFS spectra at 0, 30, 60, and 100 mAh/g as well as at max. capacity and after discharge. **d–f** Operando Ag K-edge spectra of pouch cell samples at 45 °C, 25 °C and 5 °C. **g–i** Fourier-transformed k^2-weighted EXAFS spectra (without phase-shift correction), shown as a qualitative visualization of the decay of Ag-metal-like local order during cycling. **j** Evolution of the main Ag–Ag peak intensity during charging, used as a qualitative indicator of Ag-metal-like peak decay rather than a quantitative structural fit. **k** XRD spectra of Ag–C electrodes recovered from disassembled pouch cells after CCCV charging to 200 mAh/g at 40 mA/g and a CV step at 4.25 V at 45 °C, 25 °C and 5 °C. XRD of the pristine electrode for comparison. **l** Phase and Li-content of detected Li–Ag phases. The stoichiometries of the alloy phases are β-(LiAg), γ_3-(Li_9Ag_4), γ_2-($Li_{10}Ag_3$) and δ-($Li_{98}Ag_2$), respectively. Cycling conditions for pouch cells: Operating pressure of 4 MPa, CCCV charge at 40 mA/g to 4.25 V, followed by a CV step until a specific current of 20 mA/g (QEXAFS) or a specific capacity of 200 mAh/g (XRD) was reached. Discharge at a specific current of 40 mA/g. Abbreviations: (Q)EXAFS, (quick-scanning) extended X-ray fine-structure spectroscopy; FT Fourier-transformed; XRD X-ray diffraction; CCCV constant current constant voltage; CV constant voltage.

temperature-fixed protocols that delivered only 33% of the capacity of alloy-activated cells.

We emphasize that our activation methodology requires no further modification of cell materials or processing to achieve low-temperature operation. This readily implementable strategy broadens the practical applicability of AL-ASSBs in cold environments and accelerates their commercialization.

Results

Pouch cell configuration and voltage profiles of half and full cells

We evaluated 12 mAh single-layer pouch cells in an Ag–C interlayer|LPSC|NCM configuration. The slurry-cast positive electrodes consisted of lithium nickel cobalt manganese oxide (NCM), Li_6PS_5Cl (LPSC) solid electrolyte, and carbon additives (NCM positive electrode + LPSC + C). The loading of the positive electrode composites was 21 mg/cm^2, equivalent to 4.3 mAh/cm^2 areal capacity. The solid electrolyte was a freestanding sheet, and the Ag–C interlayer had an Ag:C mass ratio of 1:3[4]. All components were stacked and pressurized by a warm isostatic press (WIP) at 500 MPa to ensure intimate interfacial contact.

Full pouch cells were cycled in climatic chambers at a mild operating pressure of 4 MPa and temperatures of 45 ± 0.5 °C, 25 ± 0.5 °C and 5 ± 0.5 °C. Electrochemical cycling tests were generally performed at 4 MPa operating pressure, constant current constant voltage charging (CCCV) and constant current (CC) discharging. Charging was done at specific currents of 40 mA/g or 0.2 C until 4.25 V, followed by a constant voltage (CV) step until the current dropped to 20 mA/g or 0.1 C. Discharging was done at a specific current of 40 mA/g. Figure 1a shows a CCP-SEM image of the full pouch cell, depicting the distinct cell layers: positive electrode composite, solid electrolyte layer, and the Ag–C interlayer adjacent to the current collector.

https://doi.org/10.1038/s41467-026-79291-1

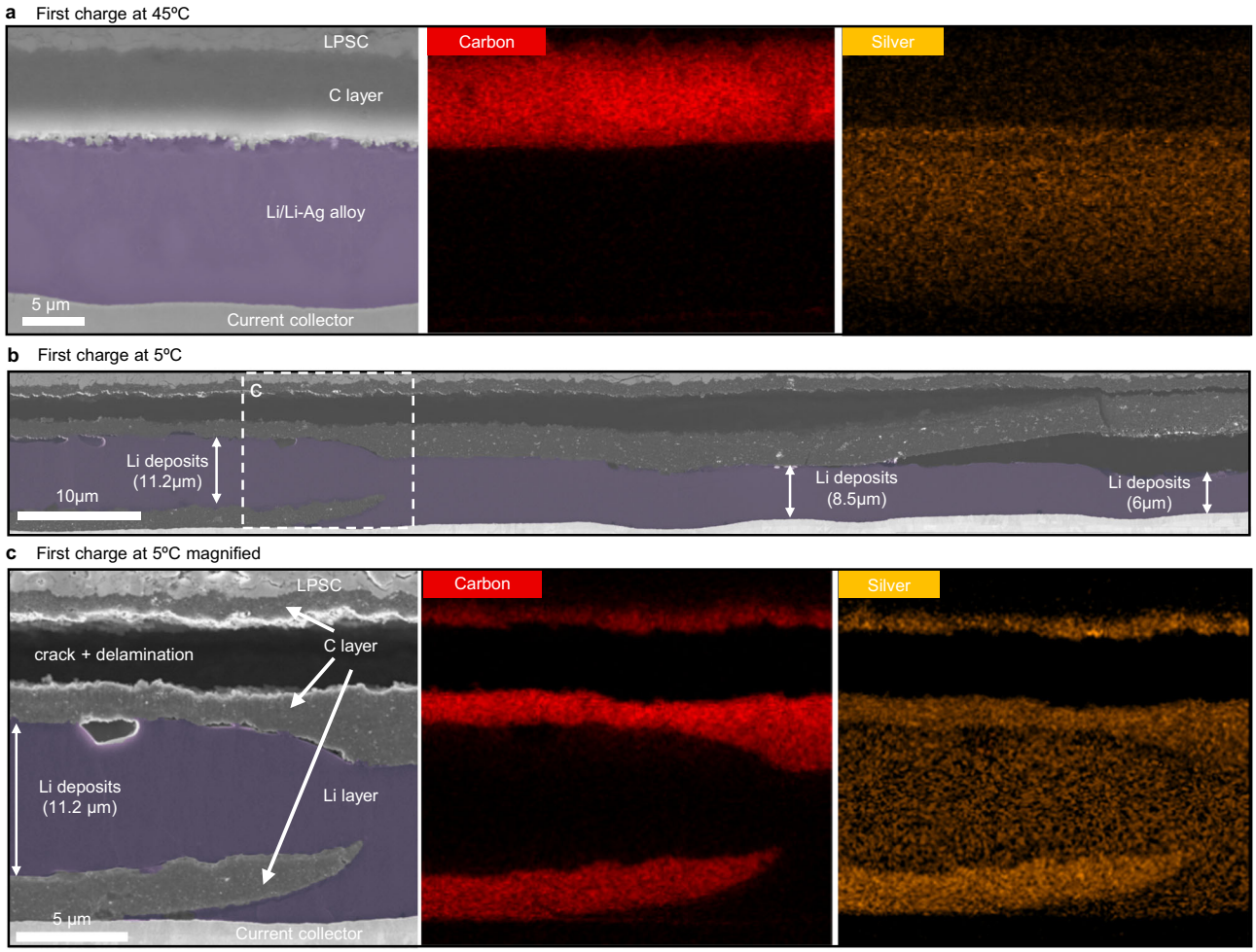


Fig. 3 | CCP-SEM/EDS of Ag–C electrodes recovered from full pouch cells after CCCV charging. a Cross-sectional SEM image and corresponding EDS elemental maps of carbon and silver after CCCV charging at 45 °C. The images show uniform lithium plating and a structurally intact Ag–C interlayer. **b** Mosaic-stitched wide-field CCP-SEM image after CCCV charging at 5 °C, revealing uneven thicknesses of lithium deposits and widespread structural degradation. **c** Magnified CCP-SEM image and corresponding carbon and silver EDS maps of the dashed box region indicated in (**b**). Specific current for all cells 40 mA/g (0.2 C); CV charging step until 20 mA/g at 4.25 V. Operating pressure: 4 MPa. Abbreviations: Ag–C silver-carbon; CCP-SEM cryogenic cross-sectional polished scanning electron microscopy; EDS energy-dispersive X-ray spectroscopy; CCCV constant-current-constant-voltage; CV constant voltage. In the EDS maps, carbon and silver are shown in red and yellow, respectively.

Energy-dispersive X-ray spectroscopy (EDS) mapping of the Ag–C interlayer (Fig. 1b) showed well-dispersed silver nanoparticles in a carbon matrix, accompanied by sulfur from the LPSC. To test temperature-dependent performance in AL-ASSBs, electrochemical tests of pouch full cells at temperatures of 45 °C, 25 °C, and 5 °C are presented in Fig. 1c. The pouch full cells exhibited significantly compromised performance at 5 °C during discharge. The observed discharge capacities were 200 mAh/g at 45 °C, decreasing to 175 mAh/g at 25 °C, and to a drastically lower 50 mAh/g at 5 °C. This decreased capacity of the pouch full cell at 5 °C also persisted in the next cycle (Fig. S1a).

To locate the origin of the sharp discharge capacity drop at 5 °C, half-cell experiments were conducted separately for the positive electrode and the Ag–C negative electrode. The first (Fig. 1d) and second cycle (Fig. S1b) discharge profiles of the positive electrode half-cells showed that they could maintain relatively stable cycling performance, despite the decrease in discharge capacity as temperatures became lower. The Ag–C half-cells, however, exhibited a significant increase in nucleation overpotential and strongly diminished discharge capacity at 5 °C. Consequently, we focused our investigation on the mechanisms in the Ag–C interlayer during low-temperature cycling, particularly on Li transport.

Operando QEXAFS

Previous studies have demonstrated that silver in Ag–C interlayers plays a key role in reversible lithium plating/stripping[4,6,10,13], with Ag-free cells performing markedly worse[4]. In particular, Li–Ag alloying appears essential for uniform lithium deposition and beneficial for facile lithium transport by lowering the diffusion barrier, which is especially critical at low temperatures where lithium diffusion is hampered[19–21]. Furthermore, alloying reactions can exhibit strong temperature sensitivity[22], which makes the link between Li–Ag alloying and Li transport even more complex. Thus, investigating alloying dynamics at temperatures in the range of ASSB applications is necessary to understand how they relate to low-temperature failure.

To selectively track the Li–Ag alloying process inside a pouch cell under realistic conditions, we performed EXAFS at the high-energy Ag K-edge (25.5 keV), circumventing interference from the rest of the pouch cell components. Our customized jig employed hard plastic plates to allow simultaneous X-ray transmission and conformal stack pressure application to the pouch cell. Proportional-integral-

derivative-controlled (PID) heating tape and Peltier cooling modules were used to precisely control the operating temperature (±1 °C; Fig. S2). For sufficient time resolution, we chose to perform QEXAFS, which can acquire one full spectrum per second. This is significantly faster than traditional EXAFS measurements, which require tens of minutes per spectrum, and enables flexible spectra merging.

The operando QEXAFS experiments were performed at three temperatures, specifically 45 ± 1 °C, 25 ± 1 °C and 5 ± 1 °C, while applying a stack pressure of 4 MPa. The voltage profiles of the pouch full cells measured during operando QEXAFS experiments (Fig. 2a–c) are consistent with those of representative pouch cells at each temperature (Fig. 1c, d).

Representative absorption spectra during cycling are shown in Fig. 2d–f. A clear trend emerged across spectra measured at different temperatures: At 45 °C, the amplitude of post-edge oscillations decreases rapidly as charging progresses, while at 25 °C a similar but less pronounced trend occurred. At 5 °C, however, pronounced fine-structure features persist over the entire charge-discharge cycle.

The corresponding k^2-weighted Fourier-transformed EXAFS (R-space) are shown in Fig. 2g–i. All initial spectra are indicative of nanosized Ag particles, in line with prior reports[23,24]. The magnitude of the Ag–Ag peak near 2.76 Å decreases most rapidly at 45 °C, more gradually at 25 °C, and only slightly at 5 °C. To qualitatively visualize the differences in alloying rate during charging at different temperatures, Fig. 2j plots R-space Ag–Ag peak intensities (peak heights normalized to the pristine 5 °C spectrum) for spectra collected up to specific capacities of 100 mAh/g. It shows distinct trends between rapid, moderate, and suppressed decay of the peak intensities for 45 °C, 25 °C, and 5 °C, respectively. Rapid attenuation of post-edge oscillations as observed at 45 °C and 25 °C indicates a fast decrease in Ag–Ag neighbors in the local atomic environment during charging. This is consistent with Ag–Li alloying, which is expected to show decreasing Ag-Ag and increasing Ag–Li coordination. Because Li is a weak scatterer, however, Ag–Li scattering is not discernible and does not overlap with the Ag–Ag peak position in our measurements. We therefore use the attenuation of the Ag–Ag peak as a qualitative indicator consistent with Ag-Li alloying during cycling, rather than as a direct quantitative measure of alloy fraction[25]. In turn, since the Ag–Li signal is not clearly resolved in our measurements, the Fourier-transformed EXAFS spectra are used here only to qualitatively track the decay of Ag–metal-like Ag–Ag correlations during charging, rather than to extract quantitative structural parameters or assign alloy phases.

In order to obtain clear phase information and to distinguish which alloy phases coexist at the relevant temperatures, we complemented the EXAFS results with XRD measurements (Fig. 2k) on cells after charging them to 200 mAh/g. Notably, we disassembled and measured the cells immediately after cycling finished to capture the phase information as close to the in situ conditions as possible. The diffraction patterns revealed that the obtained alloy phases depend on the operating temperature. At 5 °C, an intense signal from metallic Ag (38.6°) is present, indicating that the amount of Ag–Li alloy is negligible. This is consistent with the trend we observed in the corresponding EXAFS results, namely that the rate of alloying was sluggish so that only negligible amounts were formed over the entire cycle. At 25 °C, the metallic Ag peak vanished, and a series of alloy phases with varying Li-content, namely β, γ_3, Li_3Ag and γ_2, appeared alongside the δ-phase[8,17,18,26]. The coexistence of γ_2, δ and Li_3Ag was expected because the metastable γ_2 phase can disproportionate into δ and Li_3Ag. Finally, at 45 °C, δ and Li_3Ag were detected, which are more Li-rich phases than those observed at 25 °C. Interestingly, we did not detect metastable γ_2 here, indicating that 45 °C favors the disproportionation of γ_2 into δ and Li_3Ag, consistent with previous work[8]. Moreover, analogous XRD measurements on samples with a pure Ag thin film (800 nm) interlayer reveal different phase distributions compared to the Ag–C composite (Fig. S3). This discrepancy is attributed to the structurally continuous Ag matrix in the pure film, which enables direct Li–Ag alloying and subsequent lithium diffusion—a process that is otherwise impeded by carbon in the composite. Ultimately, this emphasizes that the alloying process is highly sensitive to local microenvironments, significantly impacting both alloying rates and the resulting stable phases at various temperatures.

The phases we thus identified at the end of charging follow a progression from low to high temperature: suppressed alloying at 5 °C (i.e. separate Ag and Li), a variety of Li–Ag phases ranging from β to γ_2 at 25 °C, and exclusively Li-rich phases at 45 °C (Fig. 2l). Furthermore, upon 25 °C and 45 °C discharge, alloying persisted; at 45 °C, both the γ_1 and Li_3Ag phases are present; at 25 °C, the γ_3 phase was additionally observed. Because no significant amount of Li–Ag alloy has formed at 5 °C, no Li–Ag phases were found after discharge either (Fig. S4)[8,17,18,26]. From both EXAFS and XRD, it can be concluded that the temperature modulates both the rate as well as the extent of lithiation of Ag particles.

Structure of the Ag–C interlayer and Li extrusion at high and low temperature

After establishing that the Li–Ag alloying kinetics are suppressed at low temperatures, we investigated how this correlates with the observed irreversible capacity loss at low temperatures. We performed comprehensive CCP-SEM and EDS analyses on fully charged and discharged pouch cells cycled at 45 °C (Fig. 3a) and 5 °C (Fig. 3b, c), representing complete and suppressed alloying conditions, respectively.

During charging under facile alloying conditions at 45 °C, lithium deposition proceeded uniformly throughout the electrode while maintaining the structural integrity of the carbon scaffold (Fig. 3a). EDS mapping showed clear separation between carbon and Ag–dispersed lithium metal layers, as previously reported[4]. After discharge at the same temperature, lithium was fully recovered with no residual lithium detected near the current collector (Fig. S5).

In contrast, charging at 5 °C, which suppresses Li–Ag alloying kinetics, triggered widespread and heterogeneous structural damage within the Ag–C layers (Fig. 3b, c). To comprehend the heterogeneous features at varying length scales, we obtained large field-of-view (FOV) mosaic images by stitching a series of high-resolution images (Fig. 3b), one of which is shown in Fig. 3c. Our multi-length-scale CCP-SEM-EDS analysis reveals several distinct consequences of low-temperature charging. Collectively, these structural failures manifested as non-uniform lithium deposit thickness in the large FOV mosaic images (Fig. 3b), where Li deposit layer thickness varied between 6.0 µm and 11.2 µm across the electrode. This variation indicates the accumulation of non-uniform stress within the Ag–C matrix, which is subsequently relieved through crack formation or delamination.

We identify three phenomena observed in the high-resolution images. First, sluggish lithium transport forced lithium nucleation and extrusion within the Ag–C matrix rather than at the current collector interface. This detrimental deposition mechanically fractured the carbon scaffold, creating isolated domains unable to participate in subsequent cycling. Correspondingly, Ag concentration in such isolated carbon domains near the current collector remains higher than that near the electrolyte layer. Second, in-plane cracks and delamination tend to form within the carbon scaffold, disconnecting ionic and electronic pathways. Third, lithium metal layers and carbon layers tend to lose structural integrity or adhesion, creating in-plane delamination and lithium metal voids near the interface with the carbon layers. While delamination could potentially occur during cross-sectioning sample preparation, it was only observed for electrodes cycled at 5 °C and not at 45 °C, confirming structural degradation within Ag–C layers owing to imperfect lithium plating.

https://doi.org/10.1038/s41467-026-79291-1

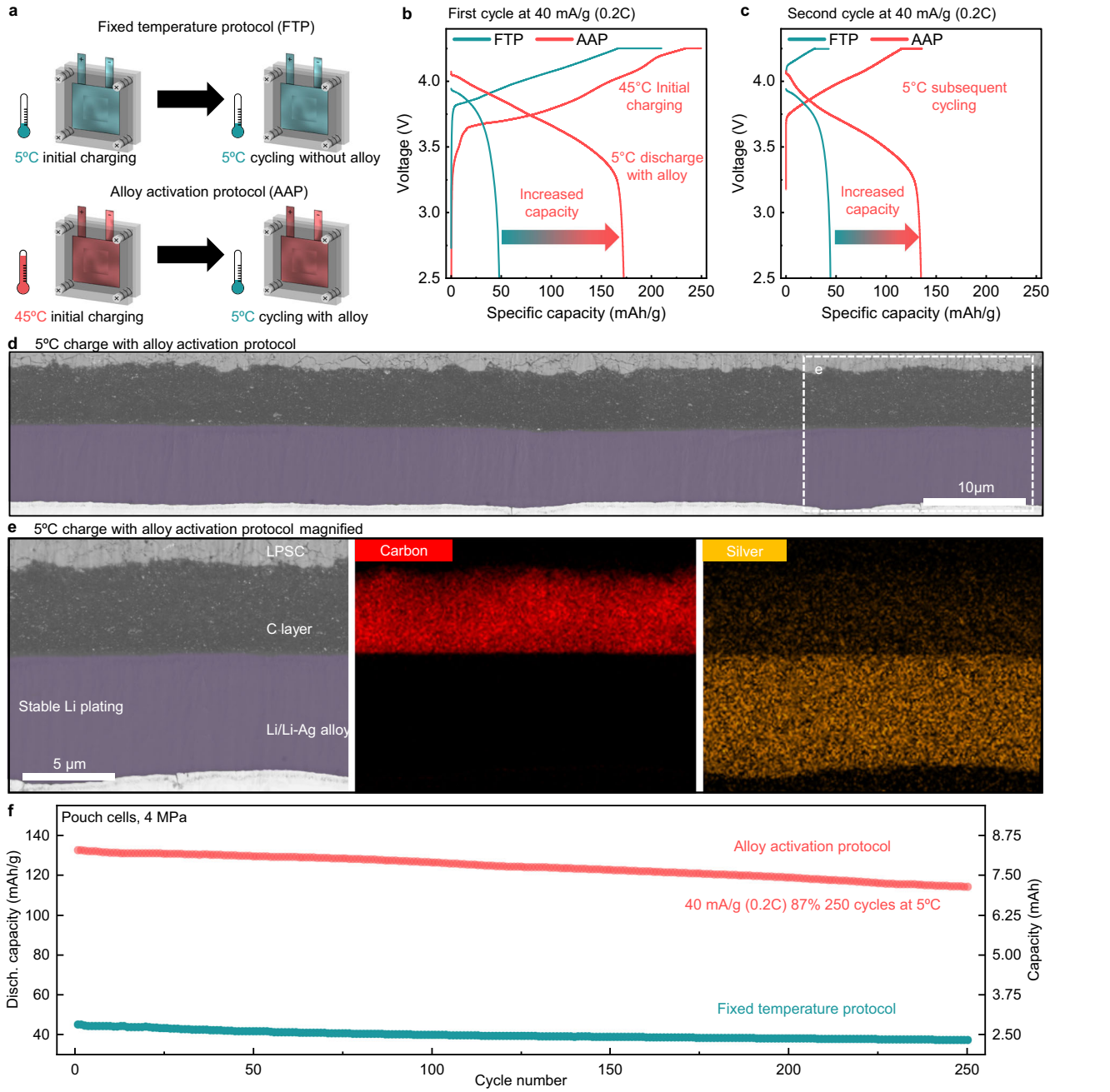


Fig. 4 | Alloy activation protocol enables stable cycling at low temperature. **a** Schematics of cycling protocols: Fixed temperature protocol (FTP) vs Alloy activation protocol (AAP). **b**, **c** First and second cycle voltage profiles of Ag–C pouch full cells with fixed temperature (5 °C) and alloy activation protocol (45–5 °C), respectively. **d** Mosaic-stitched CCP-SEM image of the Ag–C interlayer after alloy activation and subsequent full charging (CCCV) at 5 °C. **e** Magnified CCP-SEM of (**d**) and corresponding EDS maps of carbon and silver. **f** Long-term cycling performance at 5 °C for FTP and AAP in pouch full cells, reaching 87% capacity retention after 250 completed cycles following one formation cycle. Specific current for all cells 40 mA/g (0.2 C), CV charging step until 20 mA/g at 4.25 V (**d**, **e**). Operating pressure: 4 MPa. Abbreviations: FTP fixed-temperature protocol; AAP alloy activation protocol; Ag–C silver-carbon; CCP-SEM cryogenic cross-sectional polished scanning electron microscopy; EDS energy-dispersive X-ray spectroscopy; CCCV constant-current-constant-voltage; CV constant voltage. Red and cyan curves denote AAP and FTP, respectively.

Cells discharged at 5 °C showed incomplete lithium recovery from the current collector and from within the fractured Ag–C layer (Fig. S6). Residual lithium layers were trapped in planar fractures in the carbon layers, accounting for the poor coulombic efficiency. This incomplete stripping results from the irreversible structural damage inflicted on the carbon scaffold interlayer during the charging process, which greatly decreases the availability of conductive pathways during subsequent discharge, ultimately leading to limited lithium utilization during consecutive cycling.

The poor performance observed at 5 °C fundamentally stems from extensive degradation of the Ag–C layer caused by suppressed Li–Ag alloying. Based on this understanding, we hypothesized that conditioning the interlayer with pre-established Li–Ag alloy phases could provide facile lithium transport pathways that persist even at low temperatures, thereby preventing internal lithium extrusion and preserving structural integrity.

To validate this approach, we applied an alloy activation protocol (AAP) that leverages temperature-dependent alloying kinetics: an

https://doi.org/10.1038/s41467-026-79291-1

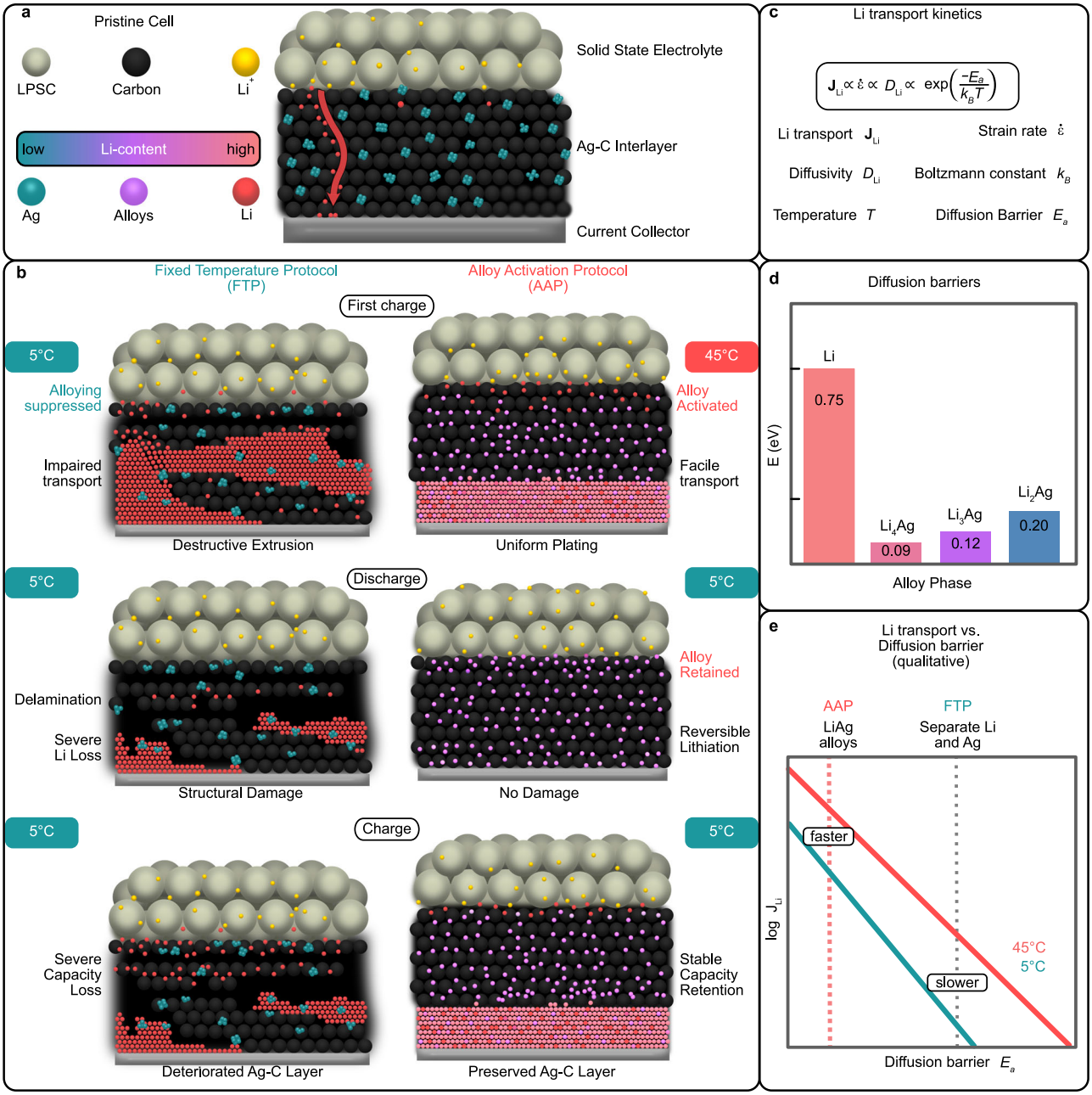


Fig. 5 | Illustration of the Ag–C interlayer dynamics. a Pristine cell composition, function and morphology. **b** Evolution of cells with fixed-temperature protocol (FTP) and alloy-activation protocol (AAP): After first charging at 5 °C (top left) and at 45 °C (top right), after discharging at 5 °C and consecutive charging at 5 °C. **c** Schematic Arrhenius scaling of lithium transport with diffusion barrier E_a and absolute temperature T for fixed geometry and driving force. **d** Diffusion barriers for Li metal and Li–Ag alloys as predicted by DFT. **e** Qualitative schematic of lithium transport versus diffusion barrier at 5 °C and 45 °C; absolute diffusivities and pre-factors were not calculated. Abbreviations and symbols: Ag–C silver-carbon; LPSC Li_6PS_5Cl solid electrolyte; FTP fixed-temperature protocol; AAP alloy activation protocol; DFT density functional theory; $\mathbf{J}_{Li}$ lithium molar flux (mol/m^{2}s); $\dot{\varepsilon}$ Coble-creep strain rate (1/s); D_{Li} lithium diffusivity (m^2/s); E_a diffusion barrier (eV per Li); k_B Boltzmann constant (8.617×10^{-5} eV/K); T absolute temperature (K). In the schematics, LPSC, carbon, Ag, Li–Ag alloys, and Li are shown in light gray, black, teal, purple, and yellow/red, respectively. The individual NEB image energies and structural snapshots supporting panel d are provided in Supplementary Figs. S11–S13 and Supplementary Data 1–4.

initial charge at 45 °C to ensure complete Ag lithiation, followed by operation at 5 °C (Fig. 4a). This strategy demonstrated dramatically enhanced low-temperature performance. Upon the first discharge at 5 °C, AAP-treated full pouch cells delivered approximately 173 mAh/g at 40 mA/g (0.2 C), whereas cells cycled exclusively at 5 °C (fixed temperature protocol, FTP) exhibited only 48 mAh/g (Fig. 4b). During the second cycle, AAP cells maintained approximately 135 mAh/g, which was comparable to the half-cell capacity at 5 °C with 134 mAh/g (Fig. 1d). This capacity reduction in the second cycle stems from increased positive electrode impedance at low temperature rather than negative electrode degradation.

Structural analysis confirmed improved transport via alloy activation. CCP-SEM analysis performed after the first discharge following alloy activation (i.e., after charging at 45 °C and then discharging at 5 °C) revealed that crack formation in the Ag–C interlayer was suppressed and lithium was stripped uniformly. This confirms that promoting initial Li–Ag alloying enables fast Li transport during

subsequent low-temperature cycling and thus preserves structural integrity (Fig. S7).

Subsequent charging at 5 °C also showed stable and homogeneous Li plating, suggesting that pre-formed Li–Ag alloys serve as persistent conduits for reversible lithium deposition even at low temperature. Mosaic-stitched CCP-SEM images further confirmed the preservation of structural integrity across wide regions of the Ag–C interlayer (Fig. 4d). High-magnification CCP-SEM/EDS (Fig. 4e) revealed intact Ag–C interfaces and well-distributed Ag within the lithium layer, indicating long-term stability of the Ag–C layer. We observed a plated Li thickness of approximately 10 µm in the CCP-SEM, which is thinner compared to 20 µm at 45 °C cycling. This difference likely reflects the lower extracted capacity due to sluggish NCM kinetics and more Li remaining in the Ag–C layer. Ex situ XRD measurements provided complementary evidence for the maintenance of alloying phases. Following AAP treatment, cells charged at 5 °C contained γ_3, γ_2, and Li_3Ag phases, while the discharged state contained γ_3 and β phases (Fig. S8), confirming that the pre-formed alloys continued to undergo reversible phase transformations even at low temperature[8,17,18,26]. Benefiting from the improved lithium transport and the structural stability of the Ag–C layer, cells cycled with the AAP achieved robust capacity retention of ~87% after 250 completed cycles following one formation cycle at 5 °C (Fig. 4f). To exclude the possibility of hidden lithium reservoirs in the Ag–C interlayer, we cycled cells with an AAP formation that started from a 45 °C discharged state (Fig. S9). With this modified protocol, cycle life is similarly improved, but due to the resulting high lithiation of the positive electrode and therefore slower kinetics, capacity is overall lower than with just a 45 °C charge.

To place the low-temperature performance of AAP-cycled Ag–C cells in context, we cycled Li|LPSC|NCM half-cells at 5 °C (Fig. S10). Their initial capacities were similar to those of the Ag–C pouch cells, consistent with a reduced interlayer transport limitation under AAP. The Ag–C cells sustained longer cycling, whereas the reference half-cells failed before 60 cycles.

To establish a mechanistic framework linking temperature-dependent alloying with electrochemical performance, we created a unified model connecting Li–Ag alloying, lithium transport kinetics, and structural integrity of the Ag–C interlayer (Fig. 5).

As established in previous studies[14,15], lithium transport through this MIEC layer occurs predominantly via Coble creep, i.e., nanoscale diffusional creep. Computational and experimental works show that in this process, lithium moves along carbon surfaces, filling the porous space between carbon particles; eventually, this results in the extrusion of lithium metal onto the current collector[16,27]. Critically, the concurrent lithiation of embedded silver nanoparticles modulates this transport process, with Li–Ag alloy formation promoting homogeneous lithium flux and uniform deposition[9,13,16].

Our comparative analysis of the FTP and AAP protocols shows how initial alloying conditions result in divergent cycling outcomes (Fig. 5b). Under FTP conditions at 5 °C, suppressed Li–Ag alloying creates regions of impeded transport within the pristine Ag–C layer. This forces local lithium extrusion within the carbon matrix, mechanically fracturing the scaffold and severing ionic/electronic pathways. The resulting structural damage manifests as incomplete lithium recovery during discharge, and subsequent cycling therefore proceeds with reduced capacity.

Conversely, the AAP strategy prevents these structural failures entirely. Pre-forming Li–Ag alloys at 45 °C establishes enhanced transport pathways that persist when temperature is lowered to 5 °C. These alloy-activated Ag–C interlayers maintain facile lithium transport to prevent internal lithium extrusion, enabling uniform lithium plating at the current collector interface even under low-temperature conditions. Additionally, the Ag–C interlayer remains stable through extended cycling, with consecutive charge-discharge cycles proceeding without structural degradation.

To explain this diverging behavior, we consider our experimental results in the context of the reported mechanistic framework: Since the incident Li^+ flux from the positive electrode is determined by the applied current density, the Li transport of the Ag–C interlayer must be fast enough to accommodate all arriving Li^+; lithium locally accumulates inside the interlayer, which is followed by local lithium extrusion[10,28]. Thus, the transport through the Ag–C interlayer ($\mathbf{J}_{Li}$) is the limiting factor that precedes facile Li extrusion towards the current collector.

The lithium transport ($\mathbf{J}_{Li}$) depends mostly on the Coble creep strain rate ($\dot{\varepsilon}$) as shown in Fig. 5c and Eq. (1):

$$\mathbf{J}_{Li} \propto \dot{\varepsilon} \propto D_{Li} \propto e^{-\frac{E_a}{k_B T}} \tag{1}$$

Here, J_{Li} is lithium molar flux (mol/m^{2}s), $\dot{\varepsilon}$ is Coble-creep strain rate (1/s), D_{Li} is lithium diffusivity (m^2/s), E_a is the calculated diffusion barrier (eV per Li), k_B is the Boltzmann constant (8.617×10^{-5} eV/K), and T is absolute temperature (in Kelvin). The proportionalities describe the temperature and barrier dependence under fixed geometry and driving force; they do not provide an absolute flux because the pre-factors were not calculated.

The strain rate itself is dependent on the diffusivity (D_{Li}), which is determined by temperature and the diffusion barrier (E_a). Regarding the latter, extensive computational studies have investigated the diffusivity of Li in Li–Ag alloys, showing that the composition strongly influences the activation energy of diffusion[20,21]. Based on these studies, we performed DFT calculations for a simplified subset of compounds (Figs. S11–S13 and Supplementary Data 1–4) consisting of pure lithium and three distinct alloy compositions (Fig. 5d). Our calculation results are consistent with the reported studies and likewise indicate that Li–Ag alloys exhibit lower diffusion barriers than pure Li, implying reduced activation energies of diffusion[29]. They further suggest that, once Li–Ag alloys have formed, the enhancement from lowered diffusion barriers may compensate for the impediment from reduced temperature, as shown in Fig. 5e. While such DFT calculations explicitly cannot model the complexity of the Ag–C system under realistic conditions, they support our rationale that lithium transport through the alloyed interlayer (as in AAP) remains sufficiently fast for facile Li extrusion even at low temperature, whereas transport through layers where Li and Ag remain unreacted (as in FTP) is expected to remain more strongly impeded.

To explore whether stack pressure can analogously improve low-temperature performance, we investigated cells cycled at an increased stack pressure of 8 MPa. This did not result in any noticeable improvement (Fig. S14). This may be because the hydrostatic pressure generated electrochemically is proposed to be orders of magnitude higher than the stack pressure (>1 GPa)[14].

Discussion

In this work, we demonstrate the low-temperature operation of anodeless Ag–C-based ASSBs through in situ alloy activation. Our work directly relates to emerging energy-intensive applications in cold-weather environments because it enables low-temperature and moderate-pressure operation while maintaining the high energy density of anodeless ASSBs in full cell configuration. Our approach requires no modifications of materials or assembly procedures, representing an easily implementable strategy for expanding the viable operating temperature range of Ag-C-based AL-ASSBs.

Comprehensive analysis including operando QEXAFS, XRD, and CCP-SEM/EDS on full pouch cells at different temperatures captured the dynamics of Li–Ag alloying. At elevated temperatures (45 °C), Li–Ag alloying proceeded rapidly, while at 5 °C it remained sluggish. By comparing cells operated at 45 °C, 25 °C, and 5 °C, we found that the

key to uniform lithium extrusion below the Ag–C layer is facile alloying dynamics, which enables fast and homogeneous lithium transport across the interlayer.

We also identified that key structural failures at low temperature occur during the initial charging cycle, where suppressed Li–Ag alloy formation leads to slow, inhomogeneous Li transport that causes internal lithium extrusion and eventual electrode delamination. Based on this, we hypothesized that a single activation cycle promoting Li–Ag alloying could provide a solution. We discovered that a one-time 45 °C charge is sufficient to activate and homogenize Li–Ag alloys. This facilitated lithium transport even at low temperatures and enabled stable subsequent cycling. Using this alloy activation protocol in full pouch cells, we achieved 87% capacity retention after 250 completed cycles following one formation cycle at 5 °C.

This work fills a substantial gap in the current body of literature where reports on the low-temperature operation of ASSBs remain scarce, especially in the context of practical full cell configurations (Table S1). Prior studies on cells employing a direct lithium-to-solid-electrolyte interface, without any interlayer, could not inform the behavior of an Ag–C composite interlayer, in which transport is governed by mixed ionic and electronic conduction and where cell failure occurs as a consequence of dendrite growth (Fig. S15). Even investigations of reactive or alloying interlayer configurations provide limited guidance, since those systems are also not MIECs and therefore operate under fundamentally different transport regimes[14]. The present work is therefore distinguished by its identification of the origin of low-temperature failure in Ag–C composite interlayers, its attribution of that failure to sluggish Li–Ag alloying and the consequent interlayer destruction as opposed to dendrite penetration into the solid-electrolyte, and its resolution of the root cause through deliberate facilitation of the alloying process. We hope that we could thus demonstrate that studies which encompass realistic operating conditions and cell configurations can yield valuable, immediately applicable insights which otherwise remain hidden.

We envision that viable low-temperature cycling of pouch-type, high-energy anodeless ASSBs will expand their use to a wider range of applications such as aerospace, electric vehicles and robotics in cold climates, and other temperature-sensitive environments. We also highlight that in situ exploitation of alloying dynamics could extend to other types of alloy-based interlayers or electrodes in ASSBs.

Methods

Preparation of the Ag–C nanocomposite layer

The Ag–C interlayer design follows Lee et al.[4]; the materials and processing conditions used here are specified below. Ag nanoparticles (Samsung SDI; 50th-percentile particle size D_{50} = 60 nm, Ag purity = 99.0% wt%, specific surface area = 6.9 m^2/g, tap density was 4.0 g/cm^3, and reported D_x = 260 Å) were blended with Asahi Carbon carbon black (D_{50} = 38 nm) at an Ag-to-carbon mass ratio of 1:3. Polyvinylidene fluoride (PVDF, Kureha) served as the binder, and N-methyl-2-pyrrolidone (NMP, Sigma-Aldrich) was added incrementally during homogenization in a planetary centrifugal mixer (AR-100, Thinky Corporation) until a coatable slurry was obtained.

The slurry was applied to 10-µm-thick Ni-Cu foil with a doctor blade. The coating was dried in air at 80 °C for 20 min and then under vacuum at 100 °C for 12 h. The finished Ag–C layer was approximately 10 µm thick and contained approximately 8 vol% Ag; the Ag loading was 8-16 mg/Ah. Preparation and handling took place in a dry room at 25 ± 1 °C with a dew point below −50 °C.

Preparation of NCM positive electrode

Lithium zirconium oxide (LZO)-coated Ni-rich NCM supplied by Samsung SDI was used as the positive electrode active material. The composite positive electrode consisted of LZO-coated NCM, sulfide solid electrolyte (<1 µm, Mitsui Mining & Smelting Co., Ltd), carbon nanotubes, and poly(vinylidene fluoride-co-hexafluoropropylene) (PVDF-HFP; M_w = 455000, Sigma-Aldrich) at a weight ratio of 85:14.5:0.5:1. Octyl acetate (99%, Sigma-Aldrich) and benzyl acetate (99%, Sigma-Aldrich), mixed at a 1:1 weight ratio, were used as the processing solvent.

The components were mixed using a planetary centrifugal mixer (AR-100, Thinky Corporation) at 2000 rpm for 45 min. The resulting slurry was doctor-blade-coated onto an aluminum current collector. The coated electrode was dried at 80 °C and subsequently vacuum-dried at 70 °C overnight. The final positive electrode sheet was approximately 100 µm thick and had an NCM areal capacity of 4.3 mAh/cm^2. All preparation and handling procedures were conducted in a dry room which was maintained at 25 ± 1°C with a dew point below −50 °C.

Preparation of SSE sheets

Freestanding solid-state electrolyte (SSE) sheets were fabricated using Li_6PS_5Cl (LPSC; purity 99 wt%, D_{50} = 3 µm, Mitsui Mining & Smelting Co., Ltd) and a non-aqueous acrylate-type binder supplied by Samsung SDI (M_w = 100000–500000; 1 wt%). Octyl acetate and benzyl acetate were combined at a 1:1 weight ratio and used as the processing solvent. LPSC and the binder were dispersed in the solvent mixture together with ZrO_2 beads (3 mm in diameter, Nikkato) using a planetary centrifugal mixer (AR-100, Thinky Corporation) at 2000 rpm for 15 min.

The resulting electrolyte slurry was doctor-blade-cast onto a 75-µm-thick polyethylene terephthalate (PET) release film. After casting, the sheet was dried in a convection oven at 80 °C and subsequently vacuum-dried at 70 °C overnight. The as-prepared SSE sheet was approximately 80 µm thick and was compressed to approximately 60 µm after cell pressurization. All preparation and handling procedures were carried out in a dry room maintained at 25 ± 1 °C with a dew point below −50 °C.

Pouch cell assembly

Single-layer, single-sided pouch cells were assembled using an NCM positive electrode, a freestanding LPSC solid electrolyte sheet, and an Ag–C-coated Ni-Cu current collector. The NCM positive electrode, LPSC sheet, and Ag–C-coated Ni-Cu current collector were cut to dimensions of 17 × 17 mm, 21 × 21 mm, and 20 × 20 mm, respectively. The three components were sequentially stacked and vacuum-sealed in an aluminum-laminated pouch.

The assembled pouch cell was subjected to warm isostatic pressing (WIP) at 500 MPa for 30 min to promote intimate contact between the constituent layers. All cell assembly procedures, except for the WIP process, were carried out in a dry room maintained at 25 ± 1 °C with a dew point below −50 °C.

Half-cell assembly and testing

Li|LPSC|Ni-rich NCM and Ag–C|LPSC|Li half cells were evaluated in uniaxial-pressure cells with a diameter of 13 mm, using the same positive electrode and Ag–C layers as in the pouch cells. First, the LPSC sheet was compressed to 380 MPa for 1 min; the electrodes were then stacked and further pressed to 500 MPa for 1 min to establish good contact. Lithium metal (99.8%, 20-µm-thick, Honjo Metal Co., Ltd.) was subsequently attached to the LPSC without additional pressure, after which a 4 MPa uniaxial stack pressure was applied for electrochemical testing. All electrodes and the LPSC were cut to 13 mm diameter disks.

Electrochemical measurements

Pouch cells were cycled using custom-made jigs to apply 4 MPa of stack operating pressure to the cells. Electrochemical experiments were performed using a battery cycler (WBCS 3000, WonA Tech) in temperature-controlled climatic chambers for 45 ± 0.5 °C, 25 ± 0.5 °C and 5 ± 0.5 °C experiments, respectively. Pouch cells were cycled at a constant current (CC) of 40 mA/g (0.2 C) in a voltage range of

2.5–4.25 V. A constant voltage (CV) charge was applied until 20 mA/g (0.1 C) was reached at 4.25 V. Discharge specific current was 40 mA/g (0.2 C).

Operando QEXAFS experiments

QEXAFS experiments were conducted at beamline BL14B2 at the Spring-8 Synchrotron and beamline 44A1 at the Taiwan Photon Source, respectively. At Spring8 BL14B2, we acquired one spectrum per 200 ms. At TPS44A1, one spectrum was acquired every 1 s. We merged spectra until the signal-to-noise ratio (S/N) was satisfactory. Data processing and analysis of the acquired QEXAFS data were performed using the ProQEXAFS[30] and Larch[31] software packages. Because the EXAFS oscillations become strongly damped upon Ag–Li alloying, particularly in more deeply lithiated states, the Fourier-transformed spectra were interpreted only qualitatively. Quantitative structural fitting and alloy-phase assignment were not performed from the FT-EXAFS data; alloy phases were instead identified independently by XRD. We used a portable Biologic SP-200 potentiostat to cycle pouch cells for operando QEXAFS. Pouch cells for operando QEXAFS experiments were cycled at 40 mA/g (0.2 C) in a voltage range of 2.5–4.25 V. A constant voltage during charging was applied until 20 mA/g (0.1 C) was reached at 4.25 V. For operando measurements, we developed a custom jig with a center perforation to apply pressure to the cell while allowing transmission mode measurements (Fig. S2). The cell was sandwiched between silicon film and hard plastic plates to apply even pressure over the entire cell. We verified that the pressure is indeed adequately distributed with pressure-sensitive paper (Fig. S1). Experiments at 25 °C were done in the air-conditioned hutch of the beamline. For experiments at elevated temperatures (45 ± 1 °C), the jig was evenly wrapped with heating coils, ensuring tight contact with the jig. Temperature measurement and control were done with a type-K thermocouple and a PID-regulated power supply, respectively. For low-temperature measurements (5 ± 1 °C), the jig assembly was placed in a Styrofoam box with Kapton windows for X-ray access. The box contents were subsequently cooled down with a commercial Peltier cooler (Scipia) attached to the top. The temperature was monitored and controlled with two Type-K thermocouples for redundancy, which provided the input for the PID-regulated power supply.

SEM experiments

SEM experiments on cross-sectioned pouch cell electrodes were conducted using a Field Emission Scanning Electron Microscope (JSM-IT800, JEOL) with acceleration voltages of 5 kV and 15 kV. The pouch cell was cut in an argon-atmosphere glovebox (<0.05 ppm water and oxygen content, Kiyeon) at 25 ± 1 °C with a razor blade (Dorco), and the cross-section was polished using a liquid-nitrogen-cooled cross-section polisher (IB-19520CCP, JEOL) at −100 °C under 6 kV to reduce sample deformation. After the sample was polished, the sample was transferred to the SEM by the JEOL Environmental Airlock system to prevent the specimen from being exposed to ambient air. EDS measurements were carried out using ULTIM MAX 170, and corresponding EDS maps were processed using Aztec (Oxford Instruments).

XRD experiments

The X-ray diffraction measurements were carried out in the 2θ range from 20° to 60° with a step size of 0.01° using an X-ray diffractometer (D8 Advance, Bruker) equipped with a Cu Kα radiation source (λ = 1.5406 Å) at 25 ± 1 °C. The Ag–C interlayer electrodes were first extracted by opening the pouch cells or uniaxial cells in the dry room (25 ± 1 °C, dew point below −50 °C). They were then scraped from the solid electrolyte layer with razor blades (Dorco) to avoid dominant LPSC signals and to expose the entire Ag–C layer to the X-ray beam. All measurements were conducted with an airtight sample holder to avoid air exposure (Bruker).

DFT calculations

All calculations were carried out using spin-polarized density functional theory (DFT) as implemented in the Vienna Ab initio Simulation Package (VASP)[32]. The Li_{sv} and Ag projector augmented-wave (PAW) pseudopotentials supplied with VASP were employed together with the Perdew-Burke-Ernzerhof (PBE) functional within the generalized gradient approximation (GGA). All structural models were taken from previously reported convex-hull phases, representing the most stable compositions[20]. Structural relaxations were performed until the residual forces were below 0.02 eV/Å and the electronic self-consistent energy was converged to 10^{-5} eV. A plane-wave cutoff of 520 eV and Γ-centered k-point meshes corresponding to 2000–3000 k-points per reciprocal atom were applied. Diffusion barriers were evaluated using the climbing-image nudged elastic band (CI-NEB) method[33] with four intermediate images. The same computational settings as in the relaxations were employed, except that a looser force threshold of 0.1 eV/Å was used for the NEB images.

Data availability

The authors declare that all data supporting the findings of this study are available within the paper and Supplementary Information files. Source data are provided with this paper.

References

1. Tang, M. et al. Low-temperature anode-free potassium metal batteries. *Nat. Commun.* **14**, 6006 (2023).
2. Heubner, C. et al. From lithium-metal toward anode-free solid-state batteries: current developments, issues, and challenges. *Adv. Funct. Mater.* **31**, 2106608 (2021).
3. Zhu, Q. et al. A 110 Wh kg^{-1} Ah-level anode-free sodium battery at −40 °C. *Joule* **8**, 482–495 (2024).
4. Lee, Y.-G. et al. High-energy long-cycling all-solid-state lithium metal batteries enabled by silver-carbon composite anodes. *Nat. Energy* **5**, 299–308 (2020).
5. Lu, Y. et al. Critical current density in solid-state lithium metal batteries: mechanism, influences, and strategies. *Adv. Funct. Mater.* **31**, 2009925 (2021).
6. Spencer-Jolly, D. et al. Structural changes in the silver-carbon composite anode interlayer of solid-state batteries. *Joule* **7**, 503–514 (2023).
7. Kamikawa, Y. Unraveling the mechanisms of lithium-alloy plating in Ag-C anode: in situ SEM study. *Adv. Sci.* **12**, 2404840 (2025).
8. Ko, D.-S. et al. Mechanism of stable lithium plating and stripping in a metal-interlayer-inserted anode-less solid-state lithium metal battery. *Nat. Commun.* **16**, 1066 (2025).
9. Lee, J.-H. et al. Lithium-silver alloys in anode-less batteries: comparison in liquid- and solid-electrolytes. *Chem. Commun.* **60**, 8268–8271 (2024).
10. Park, S. H., Naik, K. G., Vishnugopi, B. S., Mukherjee, P. P. & Hatzell, K. B. Lithium kinetics in Ag-C porous interlayer in reservoir-free solid-state batteries. *Adv. Energy Mater.* **15**, 2405129 (2025).
11. Jung, Y.-C. et al. On-site formation of silver-decorated carbon as an anodeless electrode for high-energy density all-solid-state batteries. *J. Mater. Chem. A* **11**, 25275–25282 (2023).
12. Yoon, S. G. et al. Synergistic evolution of alloy nanoparticles and carbon in solid-state lithium metal anode composites at low stack pressure. *ACS Nano* **18**, 20792–20805 (2024).
13. Wu, C. et al. Understanding the chemomechanical function of the silver-carbon interlayer in sheet-type all-solid-state lithium-metal batteries. *Nano Lett.* **23**, 4415–4422 (2023).
14. Chen, Y. et al. Li metal deposition and stripping in a solid-state battery via Coble creep. *Nature* **578**, 251–255 (2020).
15. Kim, K. H. et al. Near-strain-free anode architecture enabled by interfacial diffusion creep for initial-anode-free quasi-solid-state batteries. *Nat. Commun.* **15**, 3586 (2024).

16. Xie, F., Diallo, M. S., Kim, H., Tu, Q. H. & Ceder, G. The microscopic mechanism of lithiation and delithiation in the Ag/C buffer layer for anode-free solid-state batteries. *Adv. Energy Mater.* **14**, 2302960 (2024).
17. Jin, S. et al. Solid-solution-based metal alloy phase for highly reversible lithium metal anode. *J. Am. Chem. Soc.* **142**, 8818–8826 (2020).
18. Li, S. et al. Unveiling the stress-buffering mechanism of deep lithiated Ag nanowires: a polymer segmental motion strategy toward ultra-robust Li metal anodes. *Adv. Funct. Mater.* **32**, 2203010 (2022).
19. Kim, S. et al. The role of interlayer chemistry in Li-metal growth through a garnet-type solid electrolyte. *Adv. Energy Mater.* **10**, 1903993 (2020).
20. Thomas, J., Behara, S. S. & Van Der Ven, A. Thermodynamic and kinetic properties of the lithium-silver system. *Chem. Mater.* https://doi.org/10.1021/acs.chemmater.4c01903 (2024).
21. Huang, Y. et al. Unlocking the potential of Li–Ag alloys: phase selection and practical application. *Energy Mater. Adv.* **5**, 0108 (2024).
22. Cheng, K. et al. On the temperature-dependent diffusion growth of ϕ-Mg5Al2Zn2 ternary intermetallic compound in the Mg-Al-Zn system. *J. Mater. Sci.* **56**, 3488–3497 (2021).
23. Montano, P. A., Schulze, W., Tesche, B., Shenoy, G. K. & Morrison, T. I. Extended x-ray-absorption fine-structure study of Ag particles isolated in solid argon. *Phys. Rev. B* **30**, 672–677 (1984).
24. Itoh, M., Tohno, S., Adachi, M., Yamamoto, T. & Tsukui, S. EXAFS study of nano-phase silver particles. *Jpn. J. Appl. Phys.* **32**, 767 (1993).
25. Bridges, F., Castillo-Torres, J., Car, B., Medling, S. & Kozina, M. EXAFS evidence for a primary Zn Li dopant in $LiNbO_3$. *Phys. Rev. B* **85**, 064107 (2012).
26. Ye, Y. et al. Solid-solution or intermetallic compounds: phase dependence of the Li-alloying reactions for Li-metal batteries. *J. Am. Chem. Soc.* https://doi.org/10.1021/jacs.3c08711 (2023).
27. Jeon, S. et al. Sonochemically prepared nanodot magnesium fluoride-based anodeless carbon substrate for simultaneously reinforcing interphasial and reaction kinetics for sulfide-based all-solid-state batteries. *Adv. Energy Mater.* **14**, 2402887 (2024).
28. Park, S. H. et al. Clarification of Li deposition behavior on anodes with a porous interlayer in Li-free all-solid-state batteries. *J. Mater. Chem. A* **10**, 21995–22006 (2022).
29. Ashby, M. *Engineering Materials: An Introduction to Their Properties and Applications*. vol. 1 (Pergamon, 1980).
30. Clark, A. H., Imbao, J., Frahm, R. & Nachtegaal, M. *ProQEXAFS*: a highly optimized parallelized rapid processing software for QEXAFS data. *J. Synchrotron Radiat.* **27**, 551–557 (2020).
31. Newville, M. Larch: an analysis package for XAFS and related spectroscopies. *J. Phys. Conf. Ser.* **430**, 012007 (2013).
32. Kresse, G. & Furthmüller, J. Efficient iterative schemes for ab initio total-energy calculations using a plane-wave basis set. *Phys. Rev. B* **54**, 11169–11186 (1996).
33. Henkelman, G., Uberuaga, B. P. & Jónsson, H. A climbing image nudged elastic band method for finding saddle points and minimum energy paths. *J. Chem. Phys.* **113**, 9901–9904 (2000).

Acknowledgments

Operando QEXAFS has been performed at TPS44A1 at the Taiwan Photon Source. Another QEXAFS has also been performed at beamline BL14B2 at the Spring-8 synchrotron. We thank Dr. Ofuchi for his valuable support. We further thank Hyelim Lee for her help in acquiring CCP-SEM/EDS data.

Author contributions

H.K. and S.K. conceived the idea and designed the experiments. J.L., J.-H.K., D.K., and Y-G.L. advised on the experimental strategy and supervised the project. K.Y. made the cell components, assembled the pouch full cells and optimized cell performance. H.K., S.K., J.K., C.-W.P., and H.-W.H. planned, prepared and performed the QEXAFS experiments, data analysis and interpretation of QEXAFS spectra. H.K., S.K., and Y.H. performed the CCP-SEM experiments. H.K. and S.K. performed the XRD and electrochemical experiments and related data analysis and interpretation. S.H. performed the DFT calculations. I.N. built and optimized the temperature control setup. H.K., S.K., and J.L. wrote the manuscript. H.K., S.K., and J.L. revised the manuscript with inputs from all authors.

Funding

This work was supported by Samsung Advanced Institute of Technology (SAIT) and by the National Research Foundation of Korea (NRF). This work was funded by the Korean government (MEST) (No. 2019R1A6A1A10073437).

Competing interests

The authors declare no competing interests.

Additional information

Supplementary information The online version contains supplementary material available at https://doi.org/10.1038/s41467-026-79291-1.

Correspondence and requests for materials should be addressed to Jun Hwan Ku or Jongwoo Lim.

Peer review information *Nature Communications* thanks Jing Lin, yixian wang and the other, anonymous reviewer(s) for their contribution to the peer review of this work. A peer review file is available.

Reprints and permissions information is available at http://www.nature.com/reprints

Publisher's note Springer Nature remains neutral with regard to jurisdictional claims in published maps and institutional affiliations.

Open Access This article is licensed under a Creative Commons Attribution 4.0 International License, which permits use, sharing, adaptation, distribution and reproduction in any medium or format, as long as you give appropriate credit to the original author(s) and the source, provide a link to the Creative Commons licence, and indicate if changes were made. The images or other third party material in this article are included in the article's Creative Commons licence, unless indicated otherwise in a credit line to the material. If material is not included in the article's Creative Commons licence and your intended use is not permitted by statutory regulation or exceeds the permitted use, you will need to obtain permission directly from the copyright holder. To view a copy of this licence, visit http://creativecommons.org/licenses/by/4.0/.

© The Author(s) 2026

This Article in Press is shared early to give you faster access to new research. It is citable and carries a permanent DOI. The final edited version will replace it automatically.